Moscow Institute of Physics and Technology
(public research university)
Landau Institute for Theoretical Physics

Low-temperature electron mobility in doped semiconductors with high dielectric constant

(Master's degree diploma)

Group M02-101L
Nazaryan Kh. G,
Research supervisor
D.Sc., Prof. Feigelman M.V.

Chernogolovka 2023

Abstract

We propose and study theoretically a new mechanism of electron-impurity scattering in doped seminconductors with large dielectric constant. It is based upon the idea of *vector* character of deformations caused in the crystalline lattice by any point defects siting asymmetrically in the unit cell. In result, local lattice compression due to the elastic deformations decay as $1/r^2$ with distance from impurity. Electron scattering (due to standard deformation potential) on such defects leads to low-temperature mobility $\mu(n)$ scaling with electron density n of the form $\mu(n) \propto n^{-2/3}$ that is close to experimental observations on a number of relevant materials. The results of the research were published in the paper [1].

Contents

Chapter 1

Introduction

A wide variety of doped semiconductors has been identified that display low-temperature mobility, denoted as $\mu(n)$, which displays an almost power-law correlation with electron density, expressed as $\mu \propto n^{-\beta}$, where the exponent β ranges between $\frac{1}{2} < \beta < 1$. This effect is observable in a range of substances, including Strontium Titanate, Potassium Tantalate, Lead Telluride, and the mixed-chalcogenide compound TlBiSSe, as detailed in numerous referenced studies [2–10; 14].

Strontium Titanate, denoted $SrTiO_3$ (or STO), is one such semiconductor, as documented in various sources [2–7]. Another semiconductor that demonstrates this behavior is Potassium Tantalate, symbolized as $KTaO_3$ (or KTO) and referenced in [8]. Lead Telluride or PbTe is yet another semiconductor where this trend is discernible [2; 9; 10]. Finally, the same behavior is observed in the mixed-chalcogenide compound TlBiSSe, as detailed in the cited reference [14].

As we move towards absolute zero, the mobility is anticipated to be influenced significantly by impurity scattering. However, determining the precise mechanism behind this scattering isn't a straightforward task. Existing literature proposes two main types of scattering: scattering by screened Coulomb potentials produced by charged impurities and scattering by short-range random potentials.

The first type, scattering by screened Coulomb potentials produced by charged impurities, is rather ubiquitous and leads [11; 12] to $\mu_{\mathrm{Coul}}(n) \propto 1/\ln(n)$. This conclusion has been derived from the common understanding that charged impurities will generate screened Coulomb potentials, resulting in electron scattering. It's worth noting that these scattering phenomena don't seem to comply with the dependence we observe in our doped semiconductors.

The second type is scattering due to short-range random potentials. These are known to result in density independent scattering cross sections σ with mean-free path approximated as $l \propto 1/(n\sigma)$. Therefore, short-range potentials lead to a mobility scaling as $\mu_{\text{short}}(n) \propto n^{-4/3}$. Despite their ubiquitous presence, they still fail to explain the observed data [2–10].

What unites these various doped semiconductors is the high dielectric constant of the corresponding undoped material, which results in remarkably weak Coulomb scattering by charged impurities. In effect, this significantly reduces the influence of such scattering on the mobility of the semiconductors.

In this manuscript, we put forward and examine a novel mechanism of electron scattering by point defects, which we have termed the *vector impurity* mechanism. This idea is founded on two key observations: firstly, all the semiconductors in question possess crystal lattices with rather complex elementary cells, which prompts lattice defects (such as a vacancy or a substitutional atom) to disrupt the symmetry of the surrounding elastic media. This disruption causes the defects to act as a microscopic "force" on the surrounding elastic media. Secondly, the elastic deformations arising from a point-like force $\mathbf{F}\delta(\mathbf{r})$ applied to an elastic media give rise to lattice deformations $\mathbf{u}(\mathbf{r})$ with a slow decay in compression, $\mathrm{div}\mathbf{u} \propto 1/r^2$ [13].

We then leverage the conventional electron-phonon deformation potential Hamiltonian, written as $H_{int} \propto (\psi^\dagger\psi)\mathrm{div}\mathbf{u}$, to find that it yields the impurity transport cross-section $\nu_{tr}(q) \propto 1/q^2$, where q stands for the transferred momentum. Upon considering a typical $q \sim k_F \sim n^{1/3}$, we promptly derive mobility $\mu(n) \propto (n\nu_{tr}k_F)^{-1} \propto n^{-2/3}$, which is rather close to the observed data [2–10].

The remainder of this manuscript will be dedicated to a thorough discussion of our approach, focusing on its application to the cases of Strontium Titanate (where certain complications emerge due to its many-band structure), as well as $KTaO_3$, PbTe, and TlBiSSe. In our study, we have undertaken a detailed analysis of this mechanism, considering the unique characteristics of each semiconductor and the peculiarities of their behaviors.

Chapter 2

Elastic deformations due to vector impurities

Within the framework of semiconductor physics, a significant interaction exists between the electrons residing in the conduction-band and the distortions of the atomic lattice. This interaction is enabled by a factor referred to as the deformation potential. It's conceivable to represent this interaction through a formulation, expressed in the following equation:

$$\hat{H}_{\text{imp}} = D_{ac} \int d\mathbf{r} \hat{\psi}^{\dagger}(\mathbf{r}) \hat{\psi}(\mathbf{r}) \text{div}\mathbf{u}(\mathbf{r}) \tag{2.1}$$

In this expression, the coupling constant is denoted by D_{ac}. Typically, the value of D_{ac} is rather large, and may reach a few electron volts. Consequently, due to the considerable magnitude of D_{ac}, it becomes crucial to examine and identify potential sources that might cause distortions in the lattice leading to non-zero compression, denoted by $\mathbf{u}$.

A simple model, widely considered in the context of an isotropic elastic medium, portrays the occurrence of a void or an "empty space". This model suggests that deformations, represented by $\mathbf{u}$, that emerge around this void result in $\text{div}\mathbf{u} = 0$, as detailed in reference [13], Problem 2 for Paragraph 7.

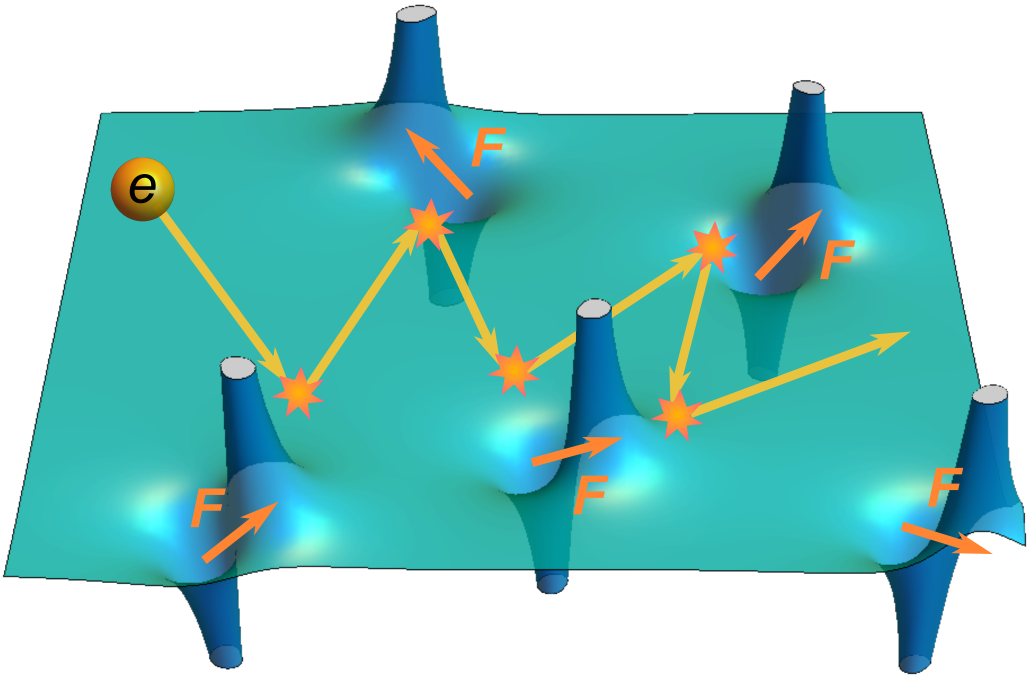

Figure 2.1: This diagram illustrates the proposed scattering mechanism in which electrons interact with a deformation potential caused by local vector impurities. These impurities, represented as local vectors **F**, alter the trajectory of electrons, as electrons can scatter by the deformation potential created by these deformation. Crucially, these vectors are randomly oriented, meaning each impurity affects the electron paths differently.

It is of paramount importance to understand that any atomic defect or anomaly within a complex crystal structure invariably disrupts the lattice's symmetry. This disruption is analogous to the presence of a local **vector** source within the structure. To illustrate this point, consider an Oxygen vacancy in STO; viewing it merely as a small spherical defect within an elastic medium would be an oversimplification. This perspective might have been applicable in the case of a vacancy in a simple cubic lattice, consisting of a single atom per unit cell. However, the reality of the lattice structure in STO is far more complex. Oxygen defects within the STO lattice are not symmetrically positioned relative to the unit cell's center. Therefore, from the viewpoint of elastic deformation symmetry, the effect of such a defect is comparable to the presence of a *frozen local force*, denoted by $\mathbf{F}$.

This concept of elastic deformations occurring in the presence of a force like $\mathbf{F}$ is not new; it was initially tackled and solved by W.Thomson back in 1848. A comprehensive solution to this problem can be found in reference [13], listed as the Problem to Paragraph 8; and for convenience detailed in the Supporting materials. The solution is presented as follows:

$$\mathbf{u} = \frac{1+\nu}{8\pi E(1-\nu)} \frac{(3-4\nu)\mathbf{F} + \mathbf{n}(\mathbf{nF})}{r} \tag{2.2}$$

In this equation, ν denotes the Poisson's ratio and E represents Young's modulus. The magnitude of the force, expressed as $F = |\mathbf{F}|$, will be utilized as a fitting parameter for our theory. This force, in essence, arises from the anisotropic local distortion of the lattice. The distortion is a result of atomic substitutions within the lattice structure. For doping concentrations that are sufficiently low, these local distortions tend to be independent of each other. Therefore, we expect the magnitude of this force

to be independent of the concentration.

As we continue our exploration, we find that the local compression, div$\mathbf{u}$, that corresponds to deformations as described by equation (2.2), can be defined as follows:

$$\nabla\mathbf{u} = \mathcal{U}\frac{\mathbf{Fr}}{r^3}, \tag{2.3}$$

$$\mathcal{U} = \frac{(1+\nu)^2}{8\pi E(1-\nu)} \tag{2.4}$$

Lastly, referring to Fig. 1, we find a graphical representation that illustrates the concept of electron scattering. This phenomenon occurs due to a random deformation potential, which in turn is caused by vector impurities within the lattice structure. This depiction provides a comprehensive understanding of the complex interactions that occur within the lattice due to various factors such as atomic defects, local forces, and atomic substitutions.

Chapter 3

Collision integral, relaxation time and mobility

Building on the foundation of the Hamiltonian (2.1), and taking into account the impurity-induced compressions as detailed in Eq.(2.4), we are now well-positioned to proceed with the calculation of electron scattering rates.

To scrutinize electrical transport within an electron system, we must make use of the Boltzmann kinetic equation. This equation will serve as a useful tool for identifying the conductivity and corresponding mobility within the context of linear response theory. The linear response theory enables us to expand the distribution function $f_{\mathbf{p}}$ as $f_{\mathbf{p}} \approx n_p + \delta n_{\mathbf{p}}$.

In this context, $n_p = [\exp(\beta\xi_p) + 1]^{-1}$ denotes the Fermi-Dirac distribution, with $\beta = 1/(k_B T)$ and the Boltzmann constant k_B. Additionally, $\xi_p = E(p) - E_F$ refers to the difference between the electron energy and the Fermi energy, represented by E_F. As we primarily focus on low-temperature transport, our discussion will exclusively revolve around situations where $k_B T \ll E_F$. Consequently, in the leading order, the Fermi-Dirac distribution can be approximated with a step function, simplifying our discussion and calculations. This permits us to write the Boltzmann equation in the presence of an electric field in its linearized form:

$$-e\mathbf{E}\mathbf{v}_{\mathbf{p}}\frac{\partial n_p\left(\xi_{\mathbf{p}}\right)}{\partial\xi_{\mathbf{p}}}=I\{\delta n_{\mathbf{p}}\} \tag{3.1}$$

Here, $\mathbf{v}_{\mathbf{p}}=\partial\xi_{\mathbf{p}}/\partial\mathbf{p}$ is the group velocity. The collision integral $I\{\delta n_{\mathbf{p}}\}$ on the right-hand side of the equation describes the electron scattering at the impurity-induced compressions which are governed by Eq.(2.4). The explicit form of the collision integral is expressed as follows:

$$I=\frac{2\pi}{\hbar}\sum_j\int_{\mathbf{p}'}|v^{(j)}_{\mathbf{p}'\mathbf{p}}|^2\left[\delta n_{\mathbf{p}'}-\delta n_{\mathbf{p}}\right]\delta\left(\varepsilon(\mathbf{p})-\varepsilon\left(\mathbf{p}'\right)\right), \tag{3.2}$$

In this equation we introduced a notation $\int_{\mathbf{p}'}=\int\frac{d^3\mathbf{p}'}{(2\pi\hbar)^3}$; the $\sum_j$ stands for a summation over impurities, and $v^{(j)}_{\mathbf{k}}$ denotes the Fourier transform of the deformation potential from the Eq.(2.4), induced by the j^{th} impurity:

$$v^{(j)}_{\mathbf{k}}=4\pi iG\frac{\mathbf{F}^{(j)}\mathbf{k}}{k^2},\quad G=\mathcal{U}D_{ac}. \tag{3.3}$$

Here, G is a new parameter encompassing all material-related properties – elastic parameters, and deformation potential. The deviation of the distribution function from the Fermi distribution is produced by the electric field. For an isotropic Fermi surface in the limit of weak electric field $\mathbf{E}$, we can preserve only the first angular harmonics and choose $\delta n_{\mathbf{p}}=\mathbf{E}\mathbf{p}\frac{\partial f}{\partial\epsilon}\eta(\varepsilon)$, with the function $\eta(\varepsilon)$ being only energy dependent.

Thus, the integral (3.2) can be explicitly evaluated, as detailed in Supporting materials, resulting in:

$$I=2\pi\frac{mG^2}{\hbar^2}\eta(\varepsilon)\frac{\partial f}{\partial\epsilon}\sum_{\text{imp}}M_{\mathbf{p}}\left(\mathbf{F}^{(j)}\right), \tag{3.4}$$

$$M_{\mathbf{p}}\left(\mathbf{F}\right)=\left(\mathbf{E}\hat{\mathbf{p}}\right)F^2-2\left(\mathbf{E}\mathbf{F}\right)\left(\mathbf{F}\hat{\mathbf{p}}\right)+3\left(\mathbf{E}\hat{\mathbf{p}}\right)\left(\mathbf{F}\hat{\mathbf{p}}\right)^2 \tag{3.5}$$

In this equation, $\hat{\mathbf{p}}$ denotes a unit vector along the momentum $\mathbf{p}$. It's important to note that the above expression depends on the relative orientation of momentum $\mathbf{p}$, the electric field $\mathbf{E}$, and the vector force $\mathbf{F}$.

Since the vector impurities are oriented randomly, in order to perform the summation over impurities, we can first average the expression (3.5) over the orientation of the vector $\mathbf{F}$, and then carry out the summation. After this, we obtain the final expression for the collision integral in the form $I = -\delta n_{\mathbf{p}}/\tau$, which gives us a relaxation time:

$$\tau = \frac{3\hbar^2 p_F}{8\pi \left(GF\right)^2 mn} \tag{3.6}$$

This relaxation time is used to find the electron mobility:

$$\mu = \frac{e\tau}{m} = \frac{3e\hbar^2 p_F}{8\pi \left(GF\right)^2 m^2 n} \tag{3.7}$$

We observe that for a concentration independent effective mass, electron mobility scales with concentration as $\mu \sim n^{-2/3}$, as was suggested in the Introduction. Nonetheless, given that mass enters in a squared form in the above equation, even a relatively weak concentration dependence $m(n)$ can considerably influence the results.

Chapter 4

Application to $SrTiO_3$

Strontium Titanate emerges as a particularly intriguing material in the context of our discussion. Although inherently a band insulator, it transitions into an extraordinarily dilute 3D metal due to minimal doping (ranging from 10^{-6} to 10^{-3} conduction electrons per unit cell) and exhibits a range of unusual properties [15–17]. These primarily stem from the close vicinity of insulating STO to a ferroelectric transition, which results in an enormous low-temperature dielectric constant $\epsilon_0 \approx 20000$. Consequently, Coulomb interaction within STO is significantly suppressed; a thorough analysis reveals that the electron mobility induced by scattering on the Coulomb field surpasses the experimental data by more than two orders of magnitude.

When lightly doped, $SrTiO_3$ exhibits an almost spherical Fermi surface. However, as concentrations exceed $n_{c1} \sim 2 \cdot 10^{18} \text{cm}^{-3}$, it evolves into a complex, far from isotropic, multiband Fermi surface [18–22]. An anisotropic Fermi surface can potentially induce correlations among successive scatterings by influencing the probability distribution of the scattering direction after each scattering event. This is notably the case for scattering on isotropic impurities where light electrons can impart a more pronounced effect on the collision integral compared to heavy ones. However, as indicated by Eq.(3.5), the collision integral heavily depends on the relative orientation of $\mathbf{p}$ and the vector force $\mathbf{F}$, as well as $\mathbf{E}$ and $\mathbf{F}$. Given that the vector forces are randomly oriented, the electron scattering is expected to be effectively averaged, and the exact shape of the Fermi surface should not be of significant importance.

This allows us to represent electron dynamics using a spherical Fermi surface, with an effective mass introduced phenomenologically as follows:

$$m = \frac{p_F^2}{2E_F} = \frac{\hbar^2 \left(3\pi^2 n\right)^{2/3}}{2E_F}, \tag{4.1}$$

Here, the Fermi energy is derived from experimental data. A somewhat similar approach is employed in [23]. The main idea behind this approximation is in substitution of the original anisotropic Fermi surface with an isotropic one with an effective mass which would produce the same Fermi energy to replace the anisotropic

Figure 4.1 summarizes various experimental data for the effective mass in STO's lowest band, obtained from different types of experiments: Shubnikov-de Haas effect, quantum oscillations, and the density of states (DoS) mass derived from specific heat measurements. The continuous green line in the same plot illustrates the $m(n)/m_0$ dependence we extracted using data from Ref.[24] for Fermi energy and Eq.(4.1), which will be used in our subsequent calculations.

The preceding discussion enables us to directly utilize the result provided by Eq.(3.7) to analyze experimental data on $SrTiO_3$. In Fig. 4.2, we compare our theoretical results for electron mobility with experimental data [3–5]. Here, we employ a single fit parameter, the strength of the vector impurity force F. The results align well with the experimental data, demonstrating a reasonable overall scaling with deviations not exceeding 10% for $n > 5 \cdot 10^{18}$ cm^{-3}.

However, our approach inaccurately predicts the mobility behavior at the lowest concentrations, where experimental data reveals a saturation of $\mu(n)$ as n decreases below $n_c \sim 5 \cdot 10^{18}$ cm^{-3}. This phenomenon is not accounted for by Eq.(3.7), implying that another scattering process must be considered to explain this feature.

One possible effect could stem from Coulomb interaction, leading to a slow logarithmic dependence of $\mu(n)$. However, a detailed analysis

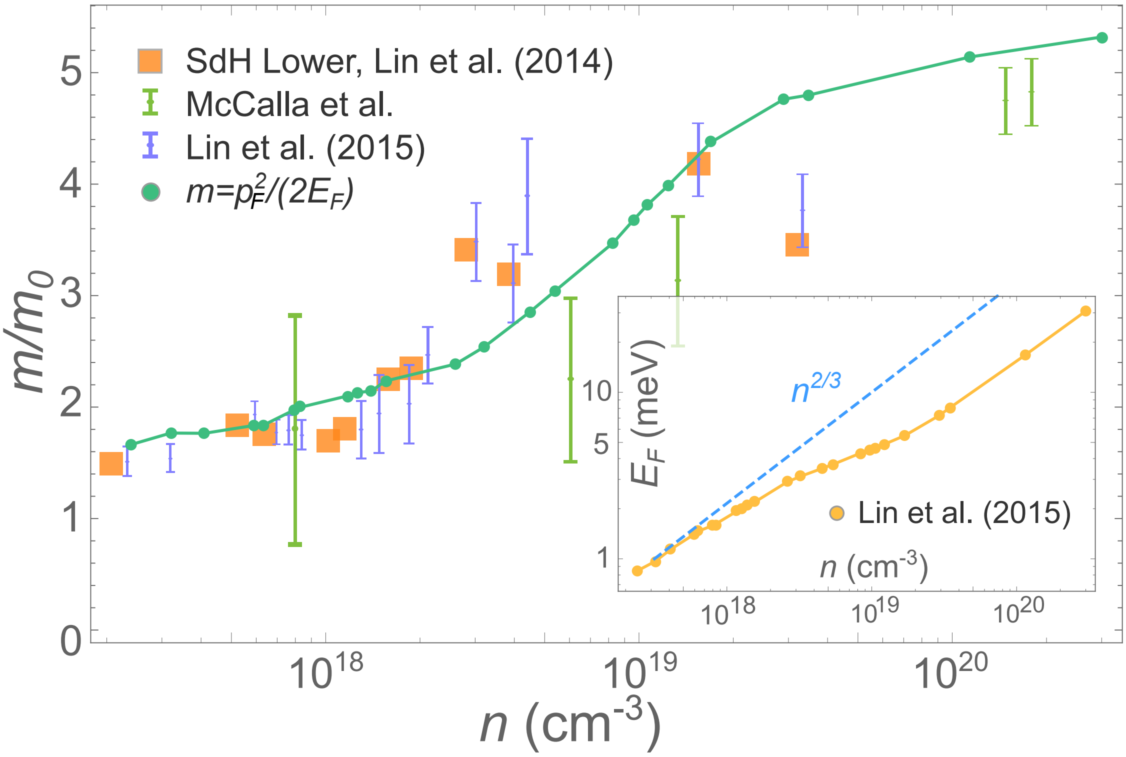

Figure 4.1: The effective mass m/m_0 (vertical) vs electron density in log scale (horizontal). Shown are the experimental values from Shubnikov-de Haas effect [18] (orange squares), from specific heat [23] (green dots), from quantum oscillations [24] (purple dots). The emerald green line showcases the $m(n)$ dependence we used, which was obtained using a model of spherical Fermi surface via Eq.(4.1). The concentration dependence of the Fermi energy is shown in the inset, see Ref. [24].

provided in the Supporting materials shows that Coulomb scattering alone would result in a mobility overestimation by two orders of magnitude.

Another possible explanation could involve electron scattering on domain walls. Such processes can be roughly modeled using a relaxation time defined as $\tau = l/v_F$, where l represents the characteristic domain size. To fit the experimental data for STO, this approach necessitates a domain size of $l \sim 0.5\mu$m. However, experimental evidence

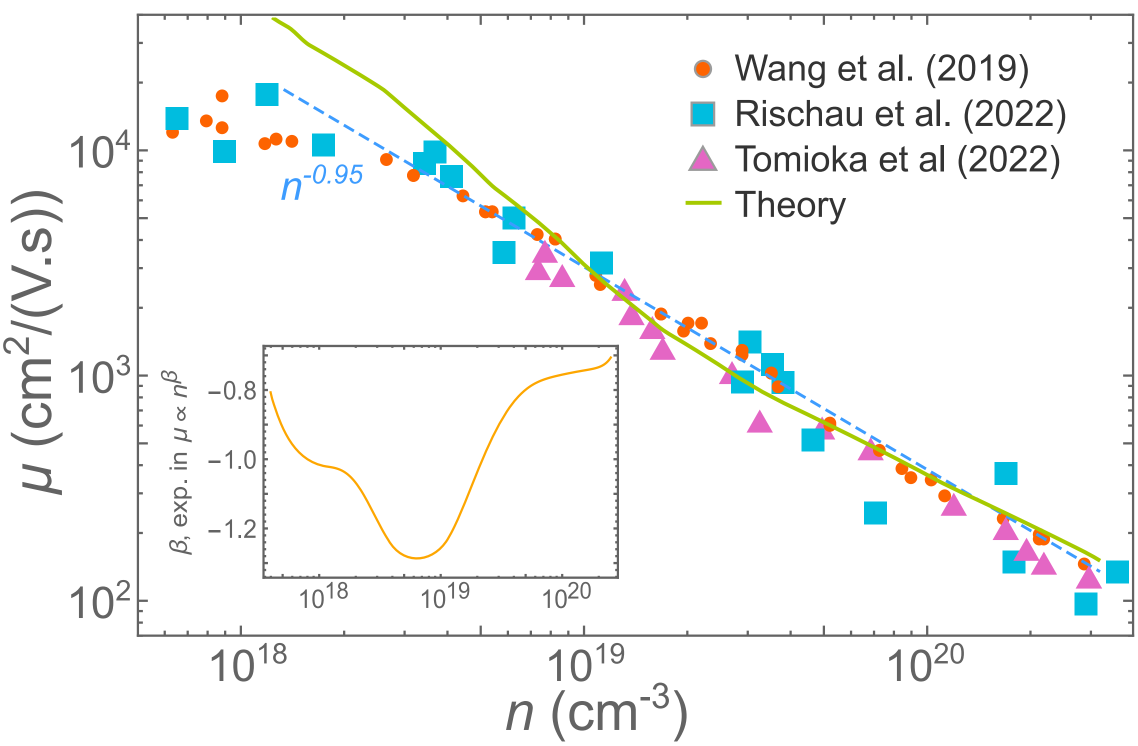

Figure 4.2: The mobility μ of STO in log scale (vertical) vs electron density in log scale (horizontal). The red circles, blue squares and magenta triangles correspond to the experimental data for $SrTiO_{3-x}$ extracted from [3–5] respectively, and the green line represents the theoretical model Eq.(3.7). The inset focuses on the local exponent $\beta = -d \ln \mu / d \ln(n)$, which varies between -0.8 and -1.2, averaging at -0.95; and the scaling $n^{-0.95}$ depicted with a dashed blue line.

[34] reveals the domain size to be an order of magnitude larger.

Lastly, we would like to mention the potential influence of spatial non-uniformity in dopant concentration as a possible cause for the observed $\mu(n)$ saturation at the lowest n. Further investigation of this issue is left for future research.

Next, we conduct a ”sanity check” to estimate the magnitude of lattice deformations induced by our vector impurities. Utilizing known parameters of $SrTiO_3$ such as the deformation potential $D_{ac} \approx 4$ eV [25], Young's modulus $E \approx 270$ GPa, and Poisson's ratio $\nu = 0.24$ [26], we can evaluate the characteristic displacement $u(a)$ at the minimal distance from the impurity. In order to describe the experimental data, we utilized a fit parameter $F \approx 9.1 \cdot 10^{-9}$ N. According to Eq. (2.2), this corresponds to the maximum atomic displacement

$$\frac{u(a)}{a} \approx 3\%, \tag{4.2}$$

where $a = 0.39$ nm is the lattice constant for $\mathrm{SrTiO_3}$. Such a maximal displacement does not appear to be unreasonable.

Chapter 5

Application to other materials

We now broaden our analysis to encompass several other doped semiconductors that possess high dielectric constants. Specifically, we utilize our methodology to investigate electron mobility in the wide-gap semiconductor perovskite Potassium Tantalate ($KTaO_3$), narrow-gap semiconductor Lead Telluride (PbTe), and the zero-gap semiconductor, a mixed-chalcogenide compound TlBiSSe. The respective dielectric constants of these materials are approximately 4500, 1000, and 20.

In PbTe, the effective electron mass is heavily dependent on the electron density [27], with a substantial increase from $0.07m_0$ at $n = 2 \cdot 10^{17}$ cm^{-3} to $0.5m_0$ at $n = 10^{20}$ cm^{-3}. The relevant data from Ref. [27] are depicted in Fig. S1 in the Supporting materials for convenience. For the calculation of the mobility dependence $\mu(n)$ in PbTe within our theory, we interpolated these actual experimental data.

As for $KTaO_3$ and TlBiSSe, we have no knowledge of any data for $m(n)$ dependencies. Therefore, we used the following constant values for these masses: $m = 0.5m_0$ [8] and $m = 0.14m_0$ [2] respectively.

To calculate mobility $\mu(n)$ dependence according to our theoretical formula (3.7), we need to use the data for the deformation potential D_{ac}, Young modulus E and Poisson ratio ν, see Eqs.(3.3) and (2.4).

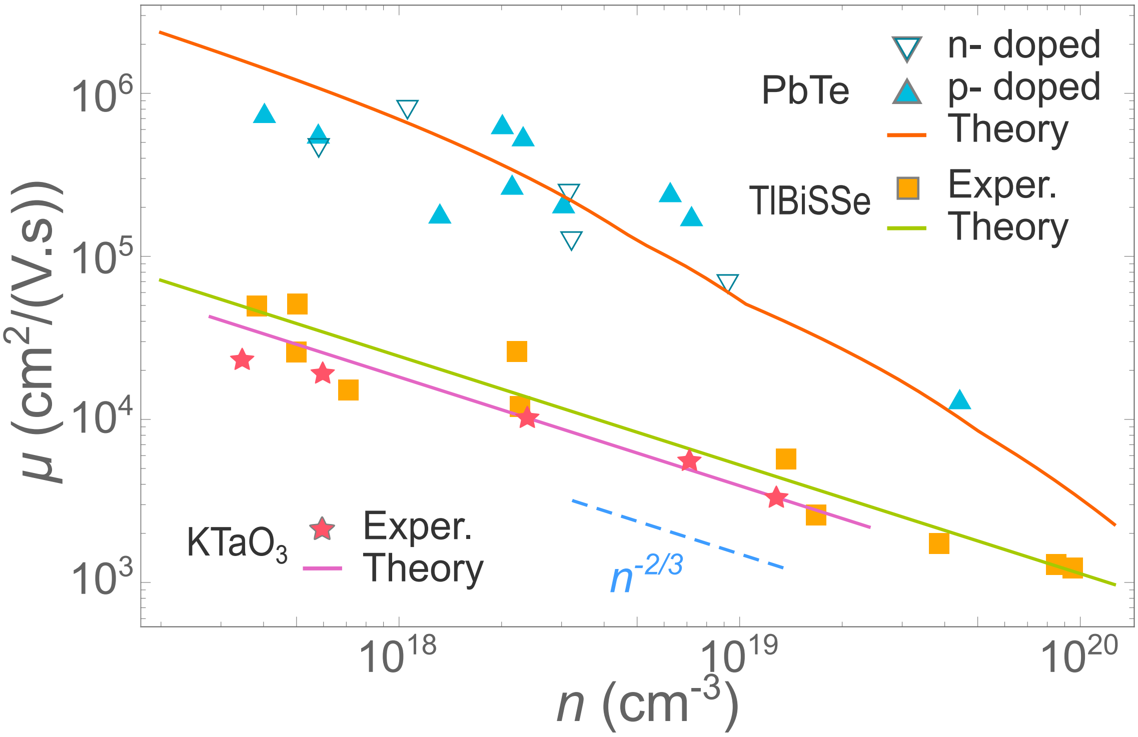

Figure 5.1: Blue triangles illustrate the data for PbTe extracted from Ref. [2; 9; 10]. The red line employs our theoretical model with the effective electron mass found in [27] (see details in the Supporting materials). The orange squares and red stars indicate the mobility data for TlBiSSe [2; 14] and $KTaO_3$ [8]. The green and pink lines represent the theoretical results for electron mobility in these materials, using constant effective masses $m = 0.14m_0$ and $m = 0.5m_0$ respectively.

For $KTaO_3$ we used $E = 215$ GPa and $\nu = 0.24$, see Ref. [28; 29]. We did not find data for the KTO deformation potential and thus used, for general orientation, the value $D_{ac} = 4$eV known for STO, as these materials are rather similar. For PbTe we used $E = 57.5$ GPa and $\nu = 0.26$, see Ref. [30], and deformation potential $D_{ac} = 15$ eV, see Ref. [31; 32].

With the material parameters mentioned above, we are left with just single unknown parameter F, the magnitude of "vector force" related to impurities in KTO and PbTe. We fit the values of this parameter to obtain best agreement between our theory and the data, the results are shown in Fig. 5.1. The overall agreement is clearly rather good, supporting the ubiquity of the proposed mechanism.

Using the values of F equal from the fit, namely $F = 2.6 \cdot 10^{-9}$ N for KTO and $F = 5.8 \cdot 10^{-10}$ N for PbTe, we estimate the analogues of Eq.(4.2), the largest relative lattice displacements $u(a)/a$ due to vector impurities. We found $u(a)/a \approx 5.5\%$ for KTO and $u(a)/a \approx 0.4\%$ for PbTe. In addition, we present in Fig. 5.1 the best fit for the $\mu(n)$ dependence in TlBiSSe. In this case we did not found the data for deformation potential and elastic modulus, thus we used for the fit the whole coefficient in front of $n^{-2/3}$ dependence.

Chapter 6

Conclusions

In this work, we proposed and developed a novel theory of electron-impurity scattering tailored specifically for materials exhibiting low electron density and high dielectric constants. The characteristic low electron density in these materials permits significant variation, across several orders of magnitude. Existing theories centered around Coulomb or short-range potentials have been unable to satisfactorily explain the empirically observed relationship between low-temperature mobility and density, $\mu(n)$, in numerous materials.

The innovative concept of vector impurities, introduced in this study, provides a fresh lens through which we can understand this peculiar type of scattering caused by the slow-decaying deformation potential.

In its most rudimentary form, our theory predicts a relationship $\mu(n) \propto n^{-2/3}$ between mobility and density. This prediction aligns reasonably well with experimental data obtained from several low-density materials. Importantly, incorporating the density-dependent effective mass $m(n)$ into our calculations yields theoretical outcomes that are in remarkably good agreement with empirical observations. We showcase these results in Fig. 4.2 for Oxygen-deficient Strontium Titanate, and in Fig. 5.1 for a range of other semiconductors, including $KTaO_3$, PbTe, and TlBiSSe.

Nevertheless, our theory has not yet fully addressed the peculiar case of Nb-substituted Strontium Titanate, which demonstrates a similar $\mu(n)$ relationship at low temperatures. It remains unclear why the substitution of a Sr atom with Nb results in the creation of a vector impurity. We recognize this as an intriguing problem worthy of future investigation.

Chapter 7

Acknowledgement

We express our gratitude to Kamran Behnia and Mikhail Glazov for their valuable discussions throughout this research. This work was funded by the Russian Science Foundation under Grant No. 21-12-00104.

Bibliography

[1] K. G. Nazaryan, M. V. Feigel'man, Low-temperature electron mobility in doped semiconductors with high dielectric constant, SciPost Phys. 14, 046 (2023), doi: 10.21468/SciPostPhys.14.3.046

[2] K. Behnia, On mobility of electrons in a shallow Fermi sea over a rough seafloor, J. Phys.: Condens. Matter 27, 375501 (2015), doi:10.1088/0953-8984/27/37/375501.

[3] J. Wang, L. Yang, C. W. Rischau, Z. Xu, Z. Ren, T. Lorenz, J. Hemberger, X. Lin and K. Behnia, Charge transport in a polar metal, npj Quantum Mater. 4, 61 (2019), doi:10.1038/s41535-019-0200-1.

[4] C. W. Rischau, D. Pulmannova, G. W. Scheerer, A. Stucky, E. Giannini and D. van der Marel, Isotope tuning of the superconducting dome of strontium titanate, Phys. Rev. Res. 4, 013019 (2022), doi:10.1103/PhysRevResearch.4.013019.

[5] Y. Tomioka, N. Shirakawa and I. H. Inoue, Superconductivity enhancement in polar metal regions of Sr0.95Ba0.05TiO3 and Sr0.985Ca0.015TiO3 revealed by systematic Nb doping, npj Quantum Mater. 7, 111 (2022), doi:10.1038/s41535-022-00524-9.

[6] H. P. R. Frederikse and W. R. Hosler, Hall mobility in SrTiO3 , Phys. Rev. 161, 822 (1967), doi:10.1103/PhysRev.161.822.

[7] A. Spinelli, M. A. Torija, C. Liu, C. Jan and C. Leighton, Electronic transport in doped SrTIO3 : Conduction mechanisms

and potential applications, Phys. Rev. B 81, 155110 (2010), doi:10.1103/PhysRevB.81.155110.

[8] S. H. Wemple, Some transport properties of oxygen-deficient single-crystal potassium tantalate (KTaO3), Phys. Rev. 137, A1575 (1965), doi:10.1103/PhysRev.137.A1575.

[9] J. D. Jensen, B. Houston and J. R. Burke, Fermi-surface parameters of p-type PbTe as a function of carrier density, Phys. Rev. B 18, 5567 (1978), doi:10.1103/PhysRevB.18.5567.

[10] R. S. Allgaier and W. W. Scanlon, Mobility of electrons and holes in PbS, PbSe, and PbTe between Room Temperature and 4.2°K, Phys. Rev. 111, 1029 (1958), doi:10.1103/PhysRev.111.1029.

[11] R. B. Dingle, Scattering of electrons and holes by charged donors and acceptors in semiconductors, Lond. Edinb. Dublin Philos. Mag. J. Sci. 46, 831 (1955), doi:10.1080/14786440808561235.

[12] C. Hamaguchi, Basic semiconductor physics, Springer, Berlin, Heidelberg, ISBN 9783662046562 (2001), doi:10.1007/978-3-662-04656-2-2.

[13] L. D. Landau and E. M. Lifshitz, Theory of elasticity: Volume 7, Elsevier, Amsterdam, Netherlands, ISBN 9780080570693 (1986), doi:10.1016/C2009-0-25521-8.

[14] M. Novak, S. Sasaki, K. Segawa and Y. Ando, Large linear magnetoresistance in the Dirac semimetal TlBiSSe, Phys. Rev. B 91, 041203 (2015), doi:10.1103/PhysRevB.91.041203.

[15] A. Spinelli, M. A. Torija, C. Liu, C. Jan and C. Leighton, Electronic transport in doped SrTiO3: Conduction mechanisms and potential applications, Phys. Rev. B 81, 155110 (2010), doi:10.1103/PhysRevB.81.155110

[16] M. N. Gastiasoro, J. Ruhman and R. M. Fernandes, Superconductivity in dilute SrTiO: A review, Ann. Phys. 417, 168107 (2020), doi:10.1016/j.aop.2020.168107

[17] C. Collignon, X. Lin, C. W. Rischau, B. Fauqué and K. Behnia, Metallicity and superconductivity in doped Strontium Titanate, Annu. Rev. Condens. Matter Phys. 10, 25 (2019), doi:10.1146/annurev-conmatphys-031218-013144.

[18] X. Lin, G. Bridoux, A. Gourgout, G. Seyfarth, S. Kramer, M. Nardone, B. Fauque and K. Behnia, Critical doping for the onset of a two-band superconducting ground state in $SrTiO_{3-\delta}$, Phys. Rev. Lett. 112, 207002 (2014), doi:10.1103/PhysRevLett.112.207002.

[19] W. Wunderlich, H. Ohta and K. Koumoto, Enhanced effective mass in doped SrTiO3 and related perovskites, Phys. B: Condens. Matter 404, 2202 (2009), doi:10.1016/j.physb.2009.04.012.

[20] M. Ahrens, R. Merkle, B. Rahmati and J. Maier, Effective masses of electrons in n-type SrTiO3 determined from low-temperature specific heat capacities, Phys. B: Condens. Matter 393, 239 (2007), doi:10.1016/j.physb.2007.01.008.

[21] K. Shirai and K. Yamanaka, Mechanism behind the high thermoelectric power factor of SrTiO3 by calculating the transport coefficients, J. Appl. Phys. 113, 053705 (2013), doi:10.1063/1.4788809.

[22] D. van der Marel, J. L. M. van Mechelen and I. I. Mazin, Common Fermi-liquid origin of T^2 resistivity and superconductivity in n-type SrTiO3 , Phys. Rev. B 84, 205111 (2011), doi:10.1103/PhysRevB.84.205111.

[23] E. McCalla, M. N. Gastiasoro, G. Cassuto, R. M. Fernandes and C. Leighton, Low-temperature specific heat of doped SrTiO3 : Doping dependence of the effective mass and Kadowaki-Woods scaling violation, Phys. Rev. Mater. 3, 022001 (2019), doi:10.1103/PhysRevMaterials.3.022001

[24] X. Lin, B. Fauqué and K. Behnia, Scalable T^2 resistivity in a small single-component Fermi surface, Science 349, 945 (2015), doi:10.1126/science.aaa8655.

[25] A. Janotti, B. Jalan, S. Stemmer and C. G. van de Walle, Effects of doping on the lattice parameter of SrTiO3, Appl. Phys. Lett. 100, 262104 (2012), doi:10.1063/1.4730998.

[26] Y. Lu, D. Jia, F. Gao, Z. Chen and T. Hu, First-principles study on the elastic properties of Sr-Ti-O ceramics, Solid State Commun. 182, 43 (2014), doi:10.1016/j.ssc.2013.12.018.

[27] I. V. Horichok and T. O. Parashchuk, Point defects in PbCdTe solid solutions, J. Appl. Phys. 127, 055704 (2020), doi:10.1063/1.5130747.

[28] Y.-Q. Xu, S.-Y. Wu, L.-J. Zhang, L.-N. Wu and C.-C. Ding, First-principles study of structural, electronic, elastic, and optical properties of cubic KNbO3 and KTaO3 crystals, Phys. Status Solidi (b) 254, 1600620 (2016), doi:10.1002/pssb.201600620.

[29] J. W. Fleming et al., Handbook of optical materials, CRC Press, Boca Raton, US, ISBN 9781315219615 (2002), doi:10.1201/9781315219615.

[30] J. E. Ni, E. D. Case, K. N. Khabir, R. C. Stewart, C.-I. Wu, T. P. Hogan, E. J. Timm, S. N. Girard and M. G. Kanatzidis, Room temperature Young's modulus, shear modulus, Poisson's ratio and hardness of PbTe-PbS thermoelectric materials, Mater. Sci. Eng.: B 170, 58 (2010), doi:10.1016/j.mseb.2010.02.026.

[31] D. M. Zayachuk, The dominant mechanisms of charge-carrier scattering in lead telluride, Semiconductors 31, 173 (1997), doi:10.1134/1.1187322.

[32] D. I. Bilc, S. D. Mahanti and M. G. Kanatzidis, Electronic transport properties of PbTe and $\mathrm{AgPb}_m\mathrm{SbTe}_{2+m}$ systems, Phys. Rev. B 74, 125202 (2006), doi:10.1103/PhysRevB.74.125202.

[33] O. N. Tufte and P. W. Chapman, Electron mobility in semiconducting strontium titanate, Phys. Rev. 155, 796 (1967), doi:10.1103/PhysRev.155.796.

[34] B. Kalisky et al., Locally enhanced conductivity due to the tetragonal domain structure in LaAlO3/SrTiO3 heterointerfaces, Nature Mater. 12, 1091 (2013), doi:10.1038/nmat3753.

[35] J. Hemberger, P. Lunkenheimer, R. Viana, R. Böhmer, and A. Loidl, Electric-field-dependent dielectric constant and nonlinear susceptibility in SrTiO3, Phys. Rev. B 52, 13159 (1995).

Chapter 8

Supporting materials

8.1 Derivation of elastic deformation

Let us determine the deformation of an infinite elastic medium when a force **F** is applied to a small region in it. If we consider the deformation at distances **r** which are large compared with the dimension of the region where the force is applied, we can suppose that the force is applied at a point. In equilibrium the internal stresses in every volume element must be balance. We can write this as

$$\frac{\partial \sigma_{ik}}{\partial x_k} + \mathbf{F}\delta(\mathbf{r}) = 0. \tag{8.1}$$

where we chose the axis origin at the point where the force is applied. Here σ_{ik} is the stress tensor and is expressed in terms of the strain tensor by

$$\sigma_{ik} = \frac{E}{1+\nu}\left(u_{ik} + \frac{\nu}{1-2\nu}u_{ii}\delta_{ik}\right). \tag{8.2}$$

And the strain tensor in its turn is expressed through the derivatives of elastic deformations as

$$u_{ik} = \frac{1}{2}\left(\frac{\partial u_i}{\partial x_k} + \frac{\partial u_k}{\partial x_i}\right) \tag{8.3}$$

Combining, we obtain the equations of equilibrium in the form

$$\frac{E}{2(1+\nu)}\frac{\partial^2 u_i}{\partial x_k^2}+\frac{E}{2(1+\nu)(1-2\nu)}\frac{\partial^2 u_l}{\partial x_i \partial x_l}+\mathbf{F}\delta(\mathbf{r})=0. \tag{8.4}$$

These equations can be more conveniently written in vector form as,

$$\Delta\mathbf{u}+\frac{1}{1-2\nu}\,\mathrm{grad}\,\mathrm{div}\,\mathbf{u}=-\frac{2(1+\nu)}{E}\mathbf{F}\delta(\mathbf{r}) \tag{8.5}$$

We look for the the solution in the form $\mathbf{u}=\mathbf{u}_0+\mathbf{u}_1$ and choose $\mathbf{u}_0$ to satisfy the Poisson-type equation:

$$\Delta\mathbf{u}_0=\frac{2(1+\nu)}{E}\mathbf{F}\delta(\mathbf{r}). \tag{8.6}$$

The solution of this equation vanishing at infinity is given as

$$\mathbf{u}_0=\frac{1+\nu}{2\pi E r}\mathbf{F} \tag{8.7}$$

We then have for $\mathbf{u}_1$ the following equation

$$\mathrm{grad}\,\mathrm{div}\,\mathbf{u}_1+(1-2\nu)\triangle\mathbf{u}_1=-\,\mathrm{grad}\,\mathrm{div}\,\mathbf{u}_0 \tag{8.8}$$

By taking the curl of this equation we obtain $\boldsymbol{\Delta}\mathbf{curl}\,\mathbf{u}_1=0$. Importantly, at infinity we must have $\mathbf{curlu}_1=0$. These two equations mean that (1) the function $\mathbf{curlu}_1$ is harmonic and (2) it vanishes at infinity. But a function harmonic in all space and zero at infinity must be zero identically. Therefore, we conclude

$$\mathbf{curl}\,\mathbf{u}_1=0 \quad\Rightarrow\quad \mathbf{u}_1=\mathbf{grad}\,\phi \tag{8.9}$$

Plugging this form into the equation (8.8), we obtain

$$\mathbf{grad}\,[2(1-\nu)\Delta\phi+\mathrm{div}\,\mathbf{u}_0]=0. \tag{8.10}$$

This equation implies that the function in the brackets is constant, and vanishes at infinity. Therefore,

$$\Delta\phi=-\frac{1}{2(1-\nu)}\mathrm{div}\,\mathbf{u}_0=-\frac{1+\nu}{4\pi E(1-\nu)}\mathbf{F}\cdot\mathbf{grad}(1/r) \tag{8.11}$$

where we used the solution for $\mathbf{u}_0$ we found in Eq. (8.7). The resulting equation can be then solved to yield an expression for $\mathbf{u}_1$ as

$$\mathbf{u}_1 = \mathbf{grad}\,\phi = \frac{1+\nu}{8\pi E(1-\nu)}\frac{(\mathbf{F}\cdot\mathbf{n})\mathbf{n}-\mathbf{F}}{r}, \quad \mathbf{n} = \frac{\mathbf{r}}{|r|}. \tag{8.12}$$

Combining, we obtain the final form of the elastic deformation in the form

$$\mathbf{u} = \frac{1+\nu}{8\pi E(1-\nu)}\frac{(3-4\nu)\mathbf{F}+\mathbf{n}(\mathbf{nF})}{r} \tag{8.13}$$

8.2 Discussions of Coulomb scattering

In this section we analyze the electron scattering by screened Coulomb (Yukawa) potential, which is expressed as

$$v(r) = \frac{Ze^2}{4\pi\epsilon_0\epsilon r}\exp\left(-r/r_{TF}\right) \tag{8.14}$$

$$\tag{8.15}$$

Here the Thomas-Fermi screening length is given by the following expression

$$r_{TF}^2 = \frac{\pi a_B^*}{4k_F}, \quad a_B^* = \frac{4\pi\epsilon_0\epsilon\hbar^2}{m^* Ze^2} \tag{8.16}$$

We then need to evaluate the collistion integral describing this scattering process. Similarly to the discussion in the main text, the latter is expressed as

$$I_{\text{imp}} = \frac{2\pi}{\hbar}\sum_{\text{imp}}\int \left|v_{\mathbf{p}'\mathbf{p}}\right|^2 \left[f\left(\mathbf{p}'\right) - f(\mathbf{p})\right]\delta\left(\varepsilon(\mathbf{p}) - \varepsilon\left(\mathbf{p}'\right)\right)\frac{d^3\mathbf{p}'}{(2\pi\hbar)^3} \tag{8.17}$$

Let us carry out a Fourier transform of the Yukawa potential to find the elements $v_{\mathbf{k}}$:

$$v_{\boldsymbol{k}} = 2\pi \int_0^\infty r^2 dr \int_0^\pi \frac{Ze^2}{4\pi\epsilon_0\epsilon r} \exp\left(-r/r_{TF}\right) e^{ikr\cos\theta} \sin\theta d\theta$$
$$= \frac{Ze^2}{\epsilon} \frac{1}{k^2 + r_{TF}^{-2}} \tag{8.18}$$

To proceed, We can again present the electron distribution function as Fermi distribution with a slight deviation.

$$f(\mathbf{p}) = n_p + f_1(\mathbf{p}) \tag{8.19}$$

Here we used f_1 as a deviation function to delineate it from the one used in the main text.

We now employ this form to rewrite the collision integral as follows,

$$I_{\text{imp}} = \frac{2\pi}{\hbar} \sum_{\text{imp}} \int \left|v_{\mathbf{p}'\mathbf{p}}\right|^2 \left[f_1\left(\mathbf{p}'\right) - f_1(\mathbf{p})\right] \delta\left(\varepsilon(\mathbf{p}) - \varepsilon\left(\mathbf{p}'\right)\right) \frac{d^3\mathbf{p}'}{(2\pi\hbar)^3} =$$
$$= \frac{2\pi}{\hbar} \sum_{\text{imp}} \int \left|v_{\mathbf{p}'\mathbf{p}}\right|^2 \left[f_1\left(\mathbf{p}'\right) - f_1(\mathbf{p})\right] \delta\left(\varepsilon(\mathbf{p}) - \varepsilon\left(\mathbf{p}'\right)\right) \frac{p'^2 \sin\theta dp' d\theta d\phi}{(2\pi\hbar)^3} \tag{8.20}$$

We will adopt the approach from our main text and focus our discussion on the isotropic problem with a concentration dependent effective mass, i.e. $\varepsilon(p) = \frac{p^2}{2m(n)}$. The isotropy allows a simplification $(f_1(\mathbf{p}) = \mathbf{p}\mathbf{E}\frac{\partial f}{\partial \varepsilon}\eta(\varepsilon))$.

Additionally, we can orient the z axis along the momentum $\mathbf{p}$, and take the momentum after scattering $\mathbf{p}'$ deflected by an angle θ relative to the z axis. The elasticity of the scattering process conserves the energy, and the isotropic Fermi surface then conserves the magnitude of momentum, $\mathbf{p} = \mathbf{p}'$. This allows to write,

$$v_{\mathbf{p}'\mathbf{p}} = \frac{Ze^2}{\epsilon_0\epsilon} \frac{1}{|\boldsymbol{p} - \boldsymbol{p}'|^2/\hbar^2 + r_{TF}^{-2}} = \frac{e^2}{\epsilon} \frac{1}{2\left(p/\hbar\right)^2 (1 - \cos\theta) + r_{TF}^{-2}} \tag{8.21}$$

Then the collision integral:

$$I_{\text{imp}} = \frac{2\pi}{\hbar}\sum_{\text{imp}}\int\left(\frac{Ze^2}{\epsilon_0\epsilon}\right)^2\frac{1}{\left(2\left(p/\hbar\right)^2\left(1-\cos\theta\right)+r_{TF}^{-2}\right)^2}\cdot$$

$$\left[\left(E_{\parallel}p'\cos\theta+E_xp'\sin\theta\cos\phi+E_yp'\sin\theta\sin\phi\right)\frac{\partial f}{\partial\varepsilon'}\eta(\varepsilon')-pE_{\parallel}\frac{\partial f}{\partial\varepsilon}\eta(\varepsilon)\right]\cdot$$

$$\cdot\,\delta\left(\frac{p^2}{2m}-\frac{p'^2}{2m}\right)\frac{mp'\sin\theta\, d\left(\frac{p'^2}{2m}\right)\, d\theta\, d\phi}{\left(2\pi\hbar\right)^3}$$

$$= -\frac{\left(2\pi\right)^2}{\hbar}\frac{\partial f}{\partial\varepsilon}\eta(\varepsilon)m\sum_{\text{imp}}\int\left(\frac{Ze^2}{\epsilon\epsilon_0}\right)^2\frac{E_{\parallel}p^2\left(1-\cos\theta\right)}{\left(2\left(p/\hbar\right)^2\left(1-\cos\theta\right)+r_{TF}^{-2}\right)^2}\cdot$$

$$\delta\left(\frac{p^2}{2m}-\frac{p'^2}{2m}\right)\frac{\sin\theta\, d\left(\frac{p'^2}{2m}\right)\, d\theta}{\left(2\pi\hbar\right)^3}$$

$$= -\frac{\left(2\pi\right)^2}{\hbar}mp\left(\frac{Ze^2}{\epsilon_0\epsilon}\right)^2\left[pE_{\parallel}\frac{\partial f}{\partial\varepsilon}\eta(\varepsilon)\right]$$

$$\sum_{\text{imp}}\int\frac{\left(1-\cos\theta\right)}{\left(2\left(p/\hbar\right)^2\left(1-\cos\theta\right)+r_{TF}^{-2}\right)^2}\frac{\sin\theta\, d\theta}{\left(2\pi\hbar\right)^3} =$$

$$= -\left(\frac{Ze^2}{\epsilon_0\epsilon}\right)^2\frac{mn}{2\pi\left(2p\right)^3}\left(-\frac{\left(2pr_{TF}/\hbar\right)^2}{\left(2pr_{TF}/\hbar\right)^2+1}+\log\left(\left(2pr_{TF}/\hbar\right)^2+1\right)\right)f_1\left(\boldsymbol{p}\right)$$

Within the relaxation time approximation, the collision integral is presented as $I = f_1(\mathbf{p})/\tau$. therefore, the zero-temperature relaxation time is expressed as

$$\tau = 2\pi\left(\frac{\epsilon_0\epsilon}{Ze^2}\right)^2\frac{\left(2p_F\right)^3}{mn}\left(-\frac{\left(2pr_{TF}/\hbar\right)^2}{\left(2pr_{TF}/\hbar\right)^2+1}+\log\left(\left(2pr_{TF}/\hbar\right)^2+1\right)\right)^{-1} \tag{8.22}$$

To obtain the final for of the relaxation time, we use the explicit expression for screening length, as $r_{TF} = \sqrt{\frac{\pi a_B^* \hbar}{4}} p_F^{-1/2}$ with $a_B^* = \frac{4\pi\epsilon\epsilon_0\hbar^2}{Zm^*e^2}$,

$$\tau = 2\pi \left(\frac{\epsilon_0\epsilon}{Ze^2}\right)^2 \frac{(2p_F)^3}{mn} \left(-\frac{\pi a_B^* p_F/\hbar}{\pi a_B^* p_F/\hbar + 1} + \log\left(\pi a_B^* p_F/\hbar + 1\right)\right)^{-1} \tag{8.23}$$

And finally, we employ the above result to derive the mobility in the following form

$$\mu = 2\pi e \left(\frac{\epsilon_0\epsilon}{Ze^2}\right)^2 \frac{(2p_F)^3}{m^2 n} \left(-\frac{\pi a_B^* p_F/\hbar}{\pi a_B^* p_F/\hbar + 1} + \log\left(\pi a_B^* p_F/\hbar + 1\right)\right)^{-1}, \tag{8.24}$$

where $a_B^* = \frac{4\pi\epsilon\epsilon_0\hbar^2}{Zm^*e^2}$.

Important to note that, if we neglect the concentration dependence of the dielectric constant, the above expression scales at low concentrations as $m\,(n)^{-2}\ln(n)$ which agrees with the scaling of experimental data surprisingly well. However, let us estimate the values for mobility predicted by the above expression. For concreteness we choose $n \approx 5 \cdot 10^{17}\text{cm}^{-3}$, and use the following values $\epsilon = 2 \cdot 10^4$, $m \approx 1.8 m_e$. For this concentrations the experimental mobility of $\text{SrTiO}_{3-\delta}$ is approximately $\mu^{\text{exp}} \approx 2\text{m}^2/(\text{V.s})$. However, the theoretical prediction overestimates the mobility value by 2 orders of magnitude, rendering this scattering mechanism inapplicable for STO.

8.3 Non-linear effects close to the Coulomb centers

In the preceding section, we observed that the scattering caused by the Coulomb potential significantly overestimated mobility, approximately two orders of magnitude, largely attributable to the considerable factor of ϵ^2 in the numerator. However, the correlation with concentration in $m(n)^{-2}\ln(n)$ is impressively favorable. This raises the question:

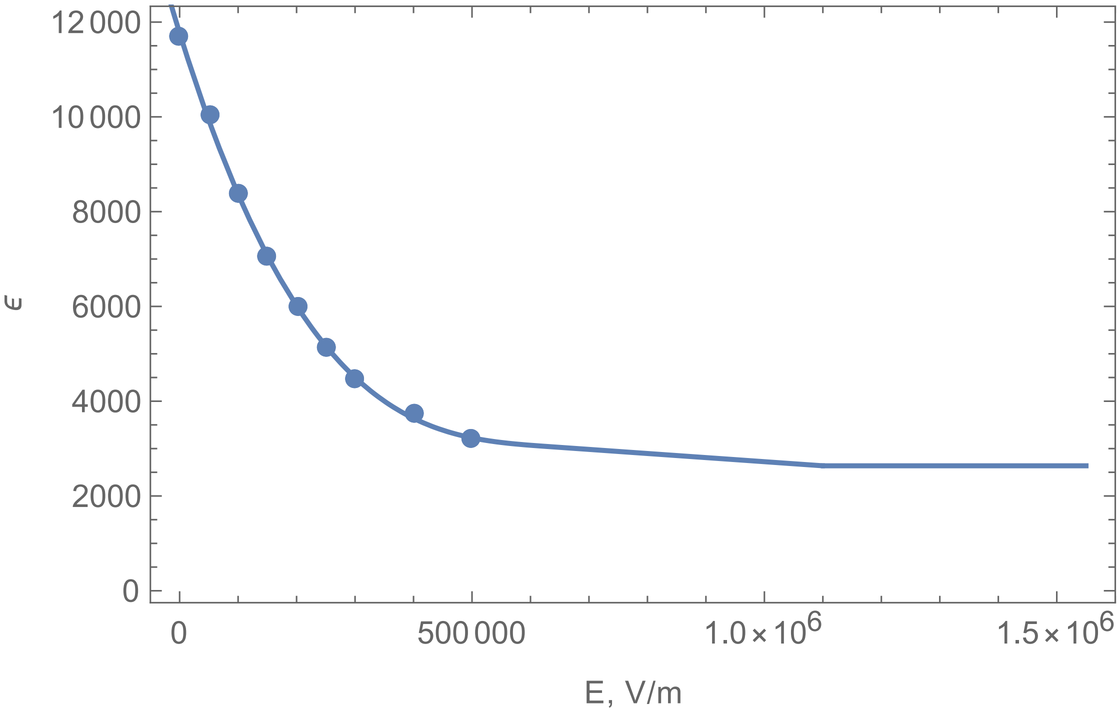

Figure 8.1: The dielectric response as a function of the bias electric field. The points are the experimental results from [35] and the line is an interpolation. In these experimental data, the value at vanishing bias fields is 12000 instaed of the well-known value 20000. We suspect that this may be due to some impurities in the sample used. However, we are not aware of any other results, thus will use them.

could there exist an underlying mechanism that results in an effective alteration of the dielectric constant?

The dielectric constant, essentially the coefficient of linear response, bridges the gap between the electrical induction within the material and the external electric field. This approximation holds true under conditions of a relatively weak electric field. However, under more general circumstances, the dielectric response is a function of the externally applied electric field, defined as:

$$\mathbf{D} = \epsilon\left(E\right)\mathbf{E} \tag{8.25}$$

In their paper, the authors [35] documented the relationship be-

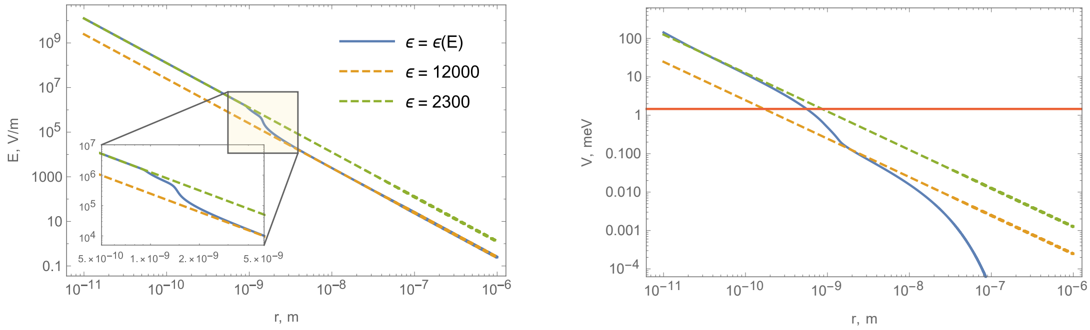

Figure 8.2: (a) Electric field as a function of the distance from the Coulomb center without the screening effect. The non-linear numerical solution interpolates between the linear response dielectric constant value $\epsilon = 12000$ at far distances to the strong field limiting value $\epsilon = 2300$. (b) Electric potential vs distance from the center accounting screening and non-linearities. The red horizontal line indicates the Fermi energy at $n = 6.3 \cdot 10^{17}\text{cm}^{-3}$.

tween the dielectric function and the bias field. We highlight their findings at zero temperature in Fig. 8.1.

To explore the potential significance of non-linear effects in the scattering process, we proceed to assess the semiclassical turning points and the associated magnitudes of the electric fields. For s- wave we can use the following estimation:

$$E_F \approx \frac{Ze^2}{4\pi\epsilon_0\epsilon r_0}\exp\left(-r_0/r_{TF}\right) \tag{8.26}$$

$$r \ll r_{TF} \Rightarrow r_0 \approx \frac{Ze^2}{4\pi\epsilon_0\epsilon E_F} \tag{8.27}$$

For $n = 4 \cdot 10^{17}\text{cm}^{-3}$, the ensuing turning point is estimated at $r_0 \approx 1.3\text{Å}$. Given its incredibly small scale, the electric fields at this point are exceptionally high, reaching approximately $E \sim 10^5\text{V/mm}$ for the same concentration near the turning point. As indicated in Fig. 8.1, the material's dielectric properties already begin to demonstrate non-linear effects at fields of 10^2V/mm. Consequently, the non-linearities have the potential to considerably alternate the results linear results.

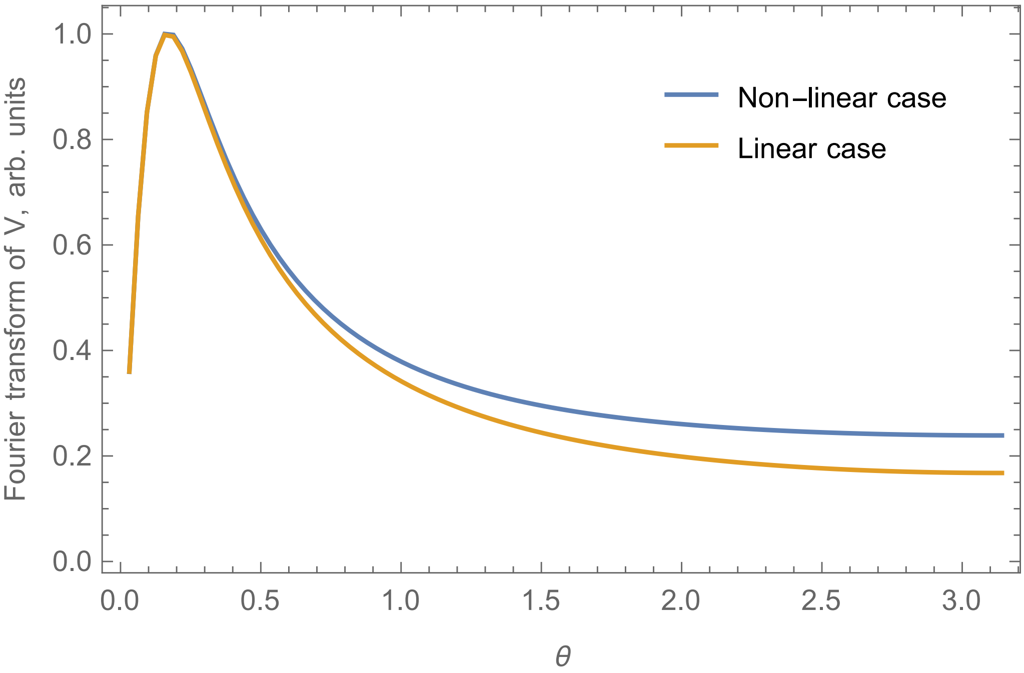

Figure 8.3: Fourier transform of the screened Coulomb potential $v_{\mathbf{p},\mathbf{p}'}$ in the linear and non-linear cases as a function of the deflection angle θ between initial and final momenta $\mathbf{p}, \mathbf{p}'$.

To compute the electric field within a non-linear framework, we apply Gauss's law, yielding

$$D = \frac{Ze}{4\pi\epsilon_0 r^2} \quad \Rightarrow \quad \epsilon(E)E = \frac{Ze}{4\pi\epsilon_0 r^2}. \tag{8.28}$$

By numerically resolving this nonlinear equation, we obtain the electric field $E(r)$, with the results presented in Fig. 8.2a). We then utilize this electric field to determine the potential $V(r)$, where we disregard the screening of the electric field within this methodology. However, we can easily reincorporate the screening aspect upon observing that non-linear effects emerge for $r \lesssim 10^{-9}$m. Comparing this value to the conventional Thomas Fermi screening length established in a linear dielectric medium reveals that $r_{TF} > 10^{-8}$m, implying that for screening effects, non-linear properties can be neglected, and we can assume that $V = V_0(r)\exp(-r/r_{TF})$. The corresponding results are illustrated in Fig. 8.2b).

Subsequently, we utilize the numerically evaluated screened non-linear Coulomb potential and execute an inverse Fourier transformation, which integrates into the collision integral. The juxtaposition of linear and non-linear outcomes is depicted in Fig. 8.3. We observe that the discrepancy between these results is at most 20%. This indicates that this methodology is not of substantial significance and fails to sufficiently modify the Coulomb scattering to accurately portray the low-concentration limit.

8.4 Collision Integral

Here we present the detailed evaluation of the collision integral, Eq.(3.2) in the main text. First, we carry out a Fourier transformation for the potential expressed through the Eq.(3.3)

$$\begin{aligned} v_{\mathbf{k}} &= 2\pi G \int_0^\infty dr \int_0^\pi F_\parallel \cos\theta e^{ikr\cos\theta} \sin\theta d\theta = \\ &= 2\pi F_\parallel \int_0^\infty dr \int_{-1}^{1} t e^{ikrt} dt = 4\pi G i \frac{(\mathbf{F}, \mathbf{k})}{k^2} \end{aligned} \tag{8.29}$$

Let us consider $\mathbf{k} = \frac{1}{\hbar}(\mathbf{p} - \mathbf{p}')$ with the z axis oriented along $\mathbf{p}$ and for sake of simplicity we recall that the investigated scattering process conserves energy, thus $|\mathbf{p}| = |\mathbf{p}'|$.

$$\begin{aligned} v_{\mathbf{p}'\mathbf{p}} &= 4\pi G i \hbar \frac{(\mathbf{F}, \mathbf{p} - \mathbf{p}')}{|\mathbf{p} - \mathbf{p}'|^2} = \\ &= 4\pi G i \hbar \frac{F_\parallel (1 - \cos\theta) - F_x \sin\theta \cos\phi - F_y \sin\theta \sin\phi}{2p(1 - \cos\theta)}, \end{aligned} \tag{8.30}$$

here the angles θ, ϕ denote the orientation of the vector $\mathbf{p}'$. Since we still have a freedom of orienting x, y axes, we can $F_y = 0$:

$$v_{\mathbf{p}'\mathbf{p}} = \frac{2\pi G i \hbar}{p} \left(F_\parallel - \frac{F_x \sin\theta \cos\phi}{(1 - \cos\theta)} \right) \tag{8.31}$$

This expression is then plugged into the collision integral, yielding

$$I_{\text{imp}} = -\frac{2\pi G^2}{\hbar}\left(\frac{\partial f}{\partial \epsilon}\eta(\epsilon)\right)\sum_{\text{imp}}\int\left(F_{\parallel} - \frac{F_x \sin\theta\cos\phi}{(1-\cos\theta)}\right)^2 \cdot \\ \cdot \left[E_{\parallel}\,(1-\cos\theta) - E_x\sin\theta\cos\phi - E_y\sin\theta\sin\phi\right]\cdot\frac{m\sin\theta\,d\theta\,d\phi}{2\pi\hbar} \tag{8.32}$$

where we have already carried out the trivial integration of the δ function. The further integration over the angles leads to the equation (3.5) from the Main text.

8.5 Effective Electron Mass in PbTe

As discussed in the main text, the effective electron mass in PbTe depends on the electron density considerably [27]: upon increasing concentration from $n = 2 \cdot 10^{17}$ cm^{-3} to $n = 10^{20}$ cm^{-3} the electron mass enhances from $0.07m_0$ up to $0.5m_0$. In Fig. 8.4 we present the experimental data from Ref. [27] as well as the interpolating function $m(n)$ which we used to evaluate the mobility.

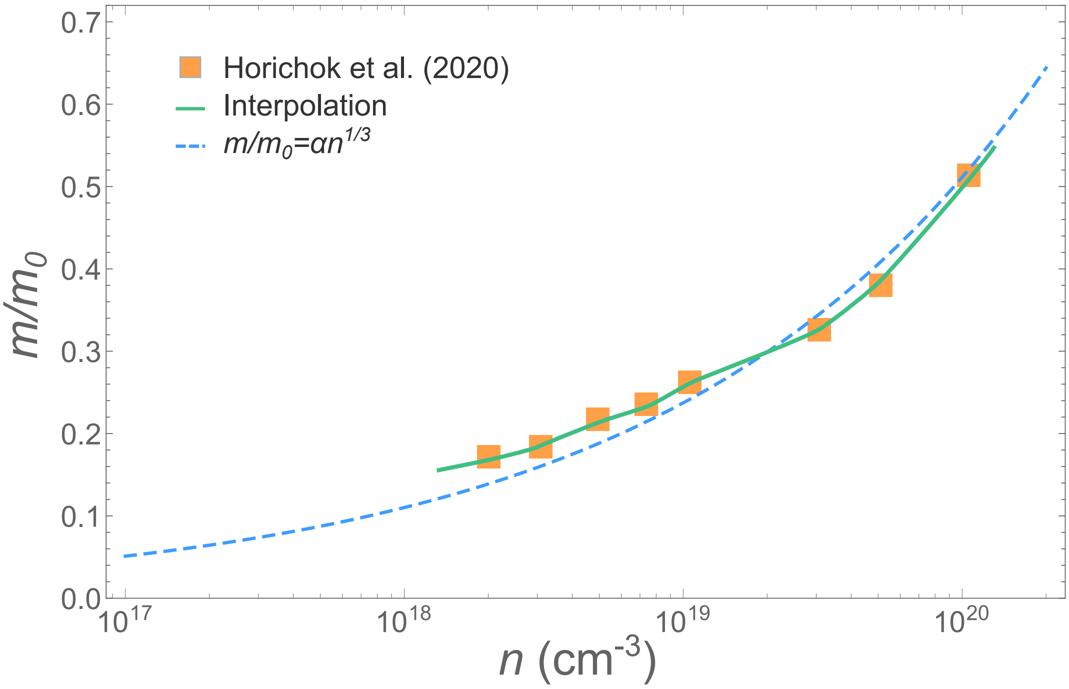

Figure 8.4: The effective mass of electrons as a function of the concentration for PbTe. The orange squares showcase the experimental data [27], the green line illustrates our interpolation employed in further calculations and the dashed blue line approximates tha data with a scaling $m/m_0 \sim \alpha n^{1/3}$ with $\alpha \approx 1.1 \cdot 10^{-7}$.